Femtosecond time-resolved dielectric function measurements by dual-angle reflectometry

C. A. D. Roeser,[a] A. M.-T. Kim, J. P. Callan, L. Huang, E. N. Glezer, Y. Siegal, and E. Mazur
Harvard University, Division of Engineering and Applied Sciences and Department of Physics, 9 Oxford Street, Cambridge, Massachusetts 02138

(Received 29 October 2002; accepted 7 April 2003)

We present a technique to measure the dielectric function of a material with femtosecond time resolution over a broad photon energy range. The absolute reflectivity is measured at two angles of incidence, and $\epsilon(\omega)$ is calculated by numerical inversion of Fresnel-like formulas. Using white-light generation, the single-color probe is broadened from the near IR to the near UV, but femtosecond time resolution is maintained. Calibration of the apparatus and error analysis are discussed. Finally, measurements of isotropic, thin film, and uniaxial materials are presented and compared to reflectivity-only studies to illustrate the merit of the technique. © *2003 American Institute of Physics.* [DOI: 10.1063/1.1582383]

I. INTRODUCTION

Ultrafast optics has blossomed into a mature but still rapidly developing field of science since subpicosecond pulses were first generated in 1976.[1] The variety of ultrafast spectroscopy techniques has grown with the development of ultrafast laser sources.[2] Many of these techniques[3,4] are exquisitely sensitive to the perturbations induced by specific excitations in material systems. At the same time, significant advances have been made in the development and commercialization of ellipsometers, a review of which is given by Collins.[5] Materials scientists have used ellipsometry as a tool to study the electronic structure of metals,[6] as a noninvasive probe of layer thicknesses and composition in multilayer stack systems,[7] and as an *in situ* monitor of thin film growth rates.[8]

Recent interest in the dynamics of highly photoexcited materials calls for measurement techniques that function as monitors of both electron and lattice dynamics. Highly excited solid state materials, especially semiconductors, are of interest for industrial applications as well as for fundamental scientific reasons. Potential applications include micromachining using femtosecond laser pulses and developments in modern high power laser diodes, in which the injection currents generate very high carrier densities. The experimental challenge in understanding the physics of high carrier densities lies in deducing the dominant process among the many that occur and in tracking the phase state of the material.

To meet this challenge, we have developed a technique that measures the dielectric function of a material with femtosecond time resolution. By measuring $\epsilon(\omega)$ with femtosecond time resolution, we can deduce the structural and electronic dynamics that occur during a photoinduced phase transition from the direct relationship between band structure and electron occupation and $\epsilon(\omega)$. Using a probe with a broad spectral range provides information at many transition energies, which reveals the redistribution of bonding strengths as the material changes phase. The dielectric function can also be used to determine the density of excited carriers and even transient carrier distributions in **k** space.

In this article, we present a dual-angle-of-incidence pump–probe reflectometry technique for measuring the femtosecond time-resolved dielectric function of a solid. In Sec. II, we discuss how this technique can be used on various solid materials. In Sec. III, we discuss the experimental details of white-light pump–probe spectroscopy. In Sec. IV, we show femtosecond time-resolved measurements of the dielectric function of GaAs, *a*-GeSb, and Te, and discuss them in relation to previous pump–probe reflectivity results.

II. DUAL-ANGLE REFLECTOMETRY METHOD

The dielectric function fully describes the linear optical properties of a material. In general, $\epsilon(\omega)$ consists of a real and an imaginary part. The imaginary part peaks at energies where the joint density of states is large, i.e., where a large number of electronic transitions are available. The real part is related to the imaginary part through the Kramers–Kronig relations and exhibits a dispersive ''wiggle'' at each absorptive peak in the imaginary part.[9]

In a crystal, there is a direct relationship between the band structure and the dielectric function.[10] Figure 1 shows the band structure and the dielectric function of GaAs. The characteristic absorption peaks in $\mathrm{Im}[\epsilon(\omega)]$ at 3.1 eV (E_1) and 4.7 eV (E_2) are due in part to a large joint densities of states around the *L* and *X* valleys, as indicated by the shaded regions in Fig. 1(a). The real part shows the characteristic dispersive structure for each absorption peak, in agreement with the Kramers–Kronig relations. The direct relationship between electronic properties and $\epsilon(\omega)$ allows monitoring of carrier dynamics through an accurate measurement of $\epsilon(\omega)$ in crystalline materials. Although **k** space cannot be defined in amorphous materials due to lack of crystal symmetry, the

[a]Electronic mail: roeser@fas.harvard.edu

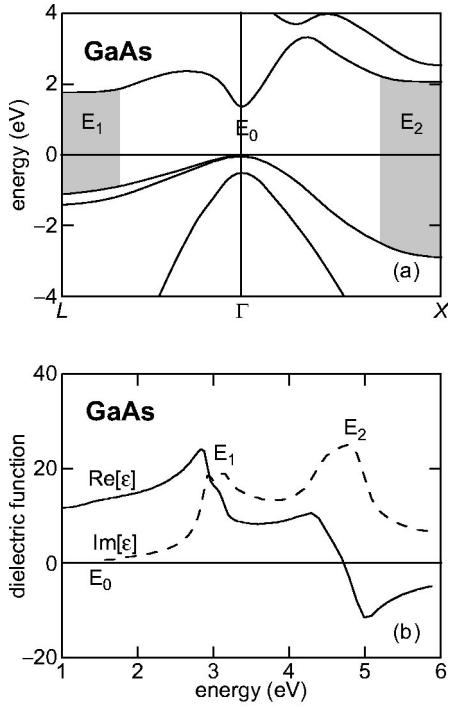

FIG. 1. (a) Band structure (see Ref. 49) and (b) dielectric function (see Ref. 32) of GaAs.

dielectric function is still determined by absorptive transitions in the material and can be used to track carrier dynamics.

The most widespread method of measuring $\epsilon(\omega)$ is ellipsometry.[11] In standard continuous wave (cw) ellipsometry, reflectivity values are typically measured at a fixed angle of incidence while the polarization of the incident light (or the orientation of a polarization analyzer) is rotated through 180°. A large number of data points allows an accurate determination of the real and imaginary part of $\epsilon(\omega)$ by inverting the Fresnel reflectivity formulas. Alternatively, the Kramers–Kronig relations between $\mathrm{Re}[\epsilon(\omega)]$ and $\mathrm{Im}[\epsilon(\omega)]$ can be used to determine the full dielectric function from the measurement of just one part. Previous experiments have measured the real part of the refractive index over a very wide frequency range,[12] and determined the imaginary part using the Kramers–Kronig relations. For an accurate calculation of the unknown quantity, it is necessary to measure the known quantity from dc to infinite frequency.

In order to measure the dielectric function of highly excited materials, we employ a dual-angle-of-incidence reflectometry technique. The finite bandwidth of the femtosecond probe prohibits using the Kramers–Kronig relations, requiring measurement of at least two quantities to determine $\mathrm{Re}[\epsilon(\omega)]$ and $\mathrm{Im}[\epsilon(\omega)]$. If one knows the structure of the sample to be investigated, two measurements are sufficient to determine $\epsilon(\omega)$. This should be contrasted with ellipsometry, where no prior knowledge of the sample is assumed and where at least three measurements are needed to determine its optical properties.[13] Although a true ellipsometry-type technique could produce results with smaller error than the technique described here, changes in the dielectric function of highly excited materials (see Sec. IV) can exceed 50% in both the real and imaginary part, which is an order of magnitude greater than the error in our apparatus. In addition, studying highly excited materials often involves pump fluences above the threshold for permanent damage of the material, where sample size limits the number of measurements that can be made. Thus, the two-angle reflectometry technique permits measurement of the dynamics of highly excited materials as over a wider range of excitation fluences and time delays than true ellipsometry without a significant sacrifice in accuracy.

In the remainder of this section, we discuss how to design a two-angle-of-incidence reflectometer. First, we consider the case of an isotropic material, then expand the discussion to include multilayer systems and anisotropic materials.

A. Determining $\epsilon(\omega)$ of isotropic materials

Because the dielectric function of a material is not directly measurable, constitutive equations are necessary to relate measurable quantities, such as reflectivity and transmissivity, to $\epsilon(\omega)$. In cw multiple-angle-of-incidence ellipsometry, measurements are performed over a range of incident angles, and $\epsilon(\omega)$ is found by numerical inversion of the appropriate constitutive equation with high accuracy and precision. For an isotropic material, the Fresnel formulas[9] are used to relate reflectivity to $\epsilon(\omega)$:

$$r_p=\frac{\epsilon\ \cos\ \theta-\sqrt{\epsilon_0}\sqrt{\epsilon-\epsilon_0\ \sin^2\ \theta}}{\epsilon\ \cos\ \theta+\sqrt{\epsilon_0}\sqrt{\epsilon-\epsilon_0\ \sin^2\ \theta}}, \tag{1}$$

$$r_s=\frac{\sqrt{\epsilon_0}\ \cos\ \theta-\sqrt{\epsilon-\epsilon_0\ \sin^2\ \theta}}{\sqrt{\epsilon_0}\ \cos\ \theta+\sqrt{\epsilon-\epsilon_0\ \sin^2\ \theta}}, \tag{2}$$

where r_p and r_s are the field reflectivities — the ratios of the reflected and incident complex E fields — for p and s polarization, respectively, and θ is the angle of incidence from medium "0." The power reflectivity R is given by the absolute square of the Fresnel factors, e.g., $R_p=|r_p|^2$. We extract both $\mathrm{Re}[\epsilon(\omega)]$ and $\mathrm{Im}[\epsilon(\omega)]$ from two measurements of the absolute reflectivity. Using the minimum number of measurements to determine $\epsilon(\omega)$ by numerical inversion requires a careful choice of operating parameters — namely, the polarization and angle of incidence.

To determine the optimum polarization and angle of incidence for the two measurements, we calculate reflectivity pairs over a range of dielectric constant values using Eqs. (1) and (2). Figure 2(a) shows a grid of dielectric constant values as well as the dielectric functions of four materials (Sb, GaAs, Si, and GeSb) over the spectral range of our probe (1.5–3.5 eV). If we choose to perform measurements at a 45° angle of incidence, p and s polarization, this grid of values is mapped into the reflectivity space shown in Fig. 2(b). With this choice operating parameters, the grid of dielectric values collapses onto a line, and so the experimental uncertainty in the measurement of absolute reflectivities will translate into a large uncertainty in dielectric constant values after numerical inversion. Although not shown here, the same problem occurs when s and p polarized reflectivity are measured at any single angle of incidence.

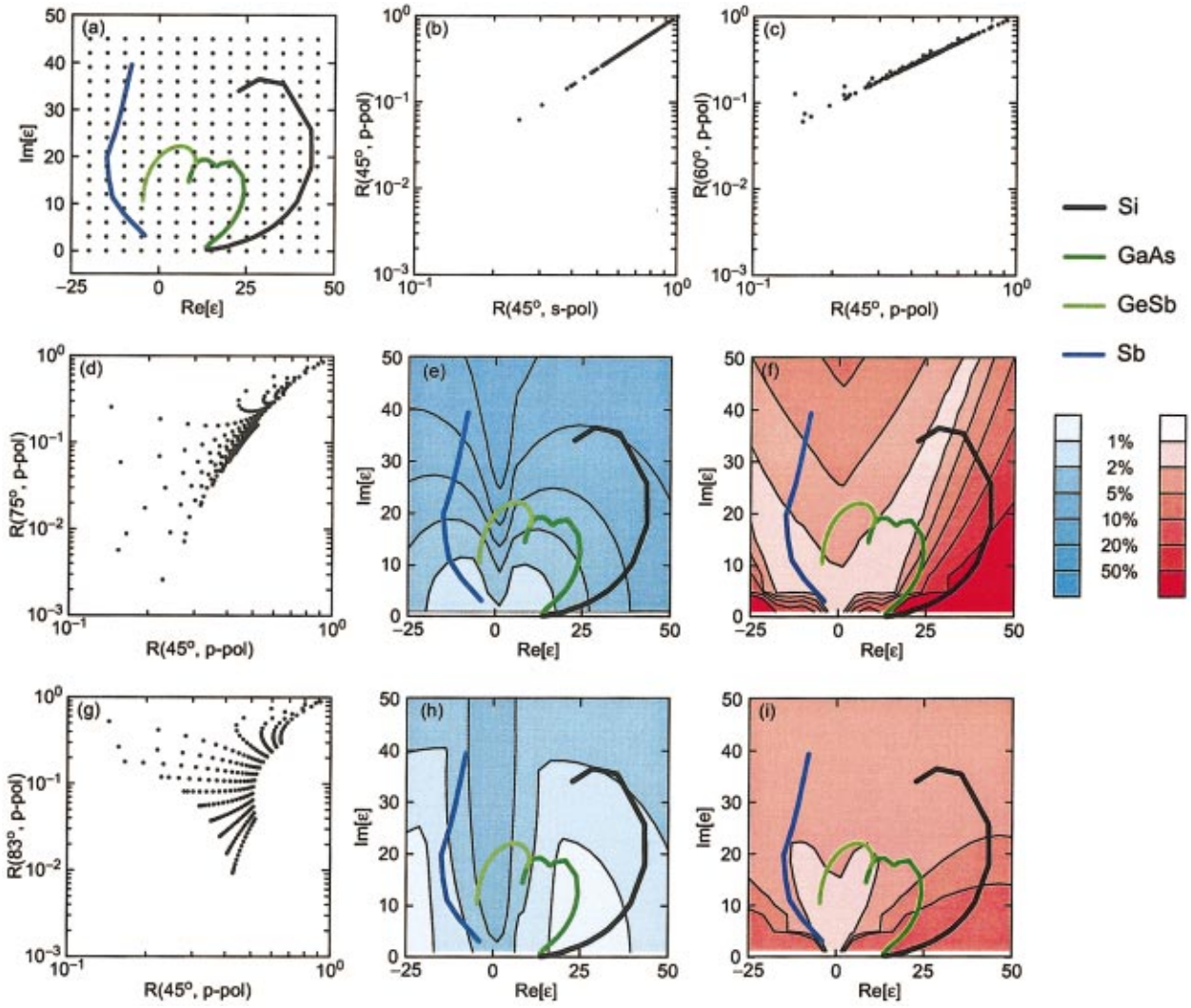

FIG. 2. (Color) (a) Dielectric functions of Si, GaAs, GeSb, and Sb (from 1.5 to 3.5 eV) are plotted over a grid of dielectric constant values. In (b), (c), (d), and (g), the Fresnel formulas are used to calculate reflectivity pairs at the angles and polarizations indicated for each of the points in (a). In (e) and (f), contour plots represent the uncertainty in extracting $\mathrm{Re}[\epsilon(\omega)]$ and $\mathrm{Im}[\epsilon(\omega)]$, respectively, given a 1% error in measuring the reflectivity for the parameters indicated in (d). Plots (h) and (i) are analogous to (e) and (f), but are calculated for the parameters indicated in (g). In all four contour plots, the representative materials are overlayed as a reference.

When both measurements are taken with *p*-polarized light at different angles of incidence, the uncertainty in extracting $\epsilon(\omega)$ can be reduced to reasonable levels. Figures 2(c), 2(d), and 2(g) show the mapping of the grid of dielectric constant values into reflectivity space for 45° angle of incidence paired with 60°, 75°, and 83°, respectively. As the second angle is increased, the grid of points in (a) spreads over a larger range of reflectivities because the pseudo-Brewster angle is approached for many of the dielectric constant values.

With the general notion of ''a good spread'' in reflectivity space in mind, we wish to fine-tune our choice of angles. In addition, we desire a sense of ''how good'' our technique can be, given a certain amount of uncertainty in measuring each reflectivity. If f is the constitutive relation between reflectivity and dielectric constant, $R=f(\epsilon,\theta)$, then

$$\begin{pmatrix}\Delta R(\theta_1)\\ \Delta R(\theta_2)\end{pmatrix}=\mathbf{J}\begin{pmatrix}\Delta\epsilon_1\\ \Delta\epsilon_2\end{pmatrix}, \tag{3}$$

where

$$\mathbf{J}=\begin{bmatrix}\dfrac{\partial f(\theta_1)}{\partial\epsilon_1} & \dfrac{\partial f(\theta_1)}{\partial\epsilon_2}\\ \dfrac{\partial f(\theta_2)}{\partial\epsilon_1} & \dfrac{\partial f(\theta_2)}{\partial\epsilon_2}\end{bmatrix} \tag{4}$$

is a Jacobian matrix and $\epsilon=\epsilon_1+i\epsilon_2$. Inverting Eq. (3) yields the uncertainty in the dielectric constant as a function of the uncertainty in reflectivity,

$$\begin{pmatrix}\Delta\epsilon_1\\ \Delta\epsilon_2\end{pmatrix}=\mathbf{J}^{-1}\begin{pmatrix}\Delta R(\theta_1)\\ \Delta R(\theta_2)\end{pmatrix}. \tag{5}$$

Assuming a 1% uncertainty in each reflectivity measurement, $\Delta R/R=0.01$, Eq. (5) predicts the uncertainty in extracting the real or imaginary dielectric constant as a function of ϵ_1 and ϵ_2. Figures 2(e) and 2(h) are contour plots of the relative uncertainty $(\Delta\epsilon_1/\epsilon_1)$ in the real part of the dielectric constant for the angles and polarizations in Figs. 2(d) and

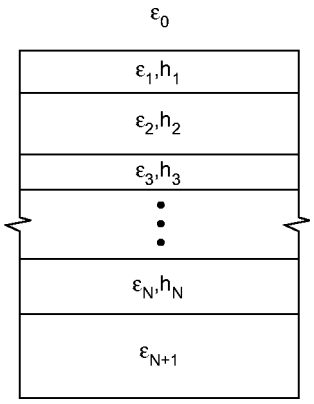

FIG. 3. Multilayer stack of N layers between the ambient (ϵ_0) and a semi-infinite substrate (ϵ_{N+1}).

2(g), respectively. The dielectric functions of the four reference materials are overlayed to show the resulting uncertainty in the dielectric functions of these materials. The decrease in error at 83° versus that at 75° is more apparent in these figures than in Figs. 2(d) and 2(g). At 75°, the uncertainty in $\mathrm{Re}[\epsilon(\omega)]$ of silicon is as much as 20%, but remains below 2% at 83°. Similar improvements are seen for the other reference materials. The uncertainty in the imaginary part of the dielectric constant also improves in going from 75° to 83°, as shown in Figs. 2(f) and 2(i). While the uncertainty is generally lower at 83° than at 75°, it does increase for certain values of (ϵ_1, ϵ_2), illustrating the fact that different angle-of-incidence pairs are optimal for different materials.

In order to find $\epsilon(\omega)$ after performing pump–probe reflectivity measurements at the chosen angles of incidence, we numerically invert the constitutive equations (in the case of an isotropic material, the Fresnel formulas). The numerical inversion algorithm is based on the simplex downhill method,[14] which minimizes the difference between the measured reflectivities and the reflectivities calculated via the constitutive equations for trial values of $\mathrm{Re}[\epsilon(\omega)]$ and $\mathrm{Im}[\epsilon(\omega)]$ at each wavelength and time delay.

B. Extension to oxide layers, thin films, and uniaxial materials

To obtain the dielectric function of an isotropic material, Eqs. (1) and (2) are required to relate $\epsilon(\omega)$ to the sample reflectivity. In practice, a single interface between the vacuum and a semi-infinite isotropic sample is rare. In this section, we introduce constitutive equations that relate the observed reflectivity to the dielectric functions of multilayer and nonisotropic materials.

1. Multilayer systems

Many solid materials develop a native oxide layer when exposed to air. Typically, native oxide layers are 1–10 nm thick with $\epsilon(\omega)$ a real constant ranging from 4 to 10 in the visible.[15] For optical experiments, especially at high angles of incidence, the native oxide layer greatly affects the reflectivity of the sample.

A general procedure for calculating the reflectivity of a multilayer stack is the matrix method described by Born and Wolf.[9] The system of interest is the multilayer stack depicted in Fig. 3. We define a characteristic matrix for each layer l,

$$M_l=\begin{bmatrix} \cos\beta_l & -\frac{i}{p_l}\sin\beta_l \\ -ip_l\sin\beta_l & \cos\beta_l \end{bmatrix}, \tag{6}$$

where

$$p_l=\sqrt{\epsilon_l-\epsilon_0\sin^2\theta_0} \tag{7}$$

and

$$\beta_l=\frac{\omega}{c}h_l p_l. \tag{8}$$

Variables ϵ_l and h_l denote the dielectric constant and thickness of layer l, respectively, and θ_0 is the angle of incidence to the stack. If there are N layers between the incident medium (labeled "0") and the substrate (labeled "$N+1$"), the characteristic matrix for the entire stack of layers is the matrix product

$$M=\prod_{l=1}^{N} M_l. \tag{9}$$

The reflectivity of the sample is calculated from the elements of the 2×2 matrix M and the optical properties of the incident medium and the substrate:[9]

$$R=|r|^2=\left|\frac{(M_{11}+M_{12}p_{N+1})p_0-(M_{21}+M_{22}p_{N+1})}{(M_{11}+M_{12}p_{N+1})p_0+(M_{21}+M_{22}p_{N+1})}\right|^2. \tag{10}$$

Equation (10) is the constitutive equation that relates the sample reflectivity to the dielectric function and thickness of each layer. For choosing angles of incidence and numerically extracting the dielectric function of a thin film or substrate, the role of Eq. (10) is identical to that of the Fresnel equations for isotropic materials, as described in Sec. II A. The layer thickness is determined by continuous wave ellipsometry or in the manner described in Sec. III B; the thickness is not determined from the numerical inversion.

2. Uniaxial materials

The crystal symmetry of an isotropic material reduces its 3×3 dielectric tensor to a single dielectric function times the identity matrix. Uniaxial, or birefringent, materials have crystal symmetries that distinguish a c axis from an ab plane. As a result, the dielectric tensor has two independent elements. The ordinary dielectric function $\epsilon_{\mathrm{ord}}(\omega)$ describes the optical properties for E fields in the ab plane while the extraordinary dielectric function $\epsilon_{\mathrm{ext}}(\omega)$ describes the optical properties for E fields along the c axis. For these materials, full optical characterization requires measuring four quantities — the real and imaginary parts of $\epsilon_{\mathrm{ord}}(\omega)$ and $\epsilon_{\mathrm{ext}}(\omega)$.

Earlier works[16,17] have derived equations for the reflectivity of uniaxial materials in various geometries. A geometry of particular interest to our technique is the following. Con-

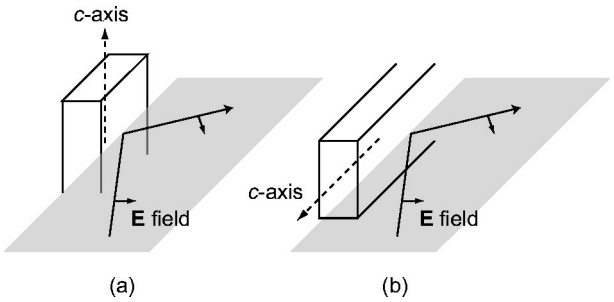

FIG. 4. Reflection configurations where the surface contains the c axis: the c axis is (a) perpendicular or (b) parallel to the plane of incidence. The E field is p polarized in both cases.

sider a three-layer structure of vacuum–oxide–substrate, where the oxide layer is isotropic but the substrate is uniaxial. The reflectivity is given by[9]

$$R=\left|\frac{r_{01}+r_{12}e^{2i\beta_1}}{1+r_{01}r_{12}e^{2i\beta_1}}\right|^2, \tag{11}$$

where r_{01} and r_{12} are the field reflectivities of the vacuum–oxide and oxide–substrate interfaces, respectively, and β_1 is calculated from Eq. (8). The vacuum–oxide reflectivity is given by the Fresnel formulas. The reflectivity of the oxide–substrate interface depends on the orientation of the c axis. If the c axis lies along the interface and is perpendicular to the plane of incidence, as in Fig. 4(a), the p-polarized reflectivity is given by Eq. (1) with $\epsilon\rightarrow\epsilon_{\mathrm{ord}}$. If the c axis lies along the interface and in the plane of incidence, as in Fig. 4(b), the p-polarized reflectivity is given by

$$r_p=\frac{n_{\|}n_{\perp}\cos\theta-n_{\mathrm{ox}}\sqrt{n_{\perp}^2-n_{\mathrm{ox}}^2\sin^2\theta}}{n_{\|}n_{\perp}\cos\theta+n_{\mathrm{ox}}\sqrt{n_{\perp}^2-n_{\mathrm{ox}}^2\sin^2\theta}}, \tag{12}$$

where $n_{\|}=\sqrt{\epsilon_{\mathrm{ext}}}$, $n_{\perp}=\sqrt{\epsilon_{\mathrm{ord}}}$, and $n_{\mathrm{ox}}=\sqrt{\epsilon_{\mathrm{ox}}}$ is the complex index of refraction of the oxide layer.

Of the possible field polarizations and c-axis orientations, the reflection geometries of Fig. 4 are the most sensitive for two-angle-of-incidence measurements of $\epsilon_{\mathrm{ord}}(\omega)$ and $\epsilon_{\mathrm{ext}}(\omega)$. For the geometry of Fig. 4(a), the reflectivity depends solely on the ordinary dielectric function. Using the same analysis as in Sec. II A, two angles of incidence are chosen and the time-resolved ordinary dielectric function is measured. Then, in the geometry of Fig. 4(b), the extraordinary part of the dielectric tensor can be extracted using Eq. (12), because the values of $\epsilon_{\mathrm{ord}}(\omega)$ have been measured for each time delay and pump fluence. In addition to being sensitive to the two dielectric functions of interest in each case, these measurement geometries have the advantage of being related by a 90° rotation of the sample.

III. EXPERIMENTAL SETUP AND CALIBRATION

The dual-angle technique described above can be used in conjunction with any femtosecond-pulse laser source to measure the dielectric constant at a single wavelength. By using a white-light pump–probe design, we maintain femtosecond time resolution while probing a broad spectral range (1.8–3.4 eV). In Sec. III A, we describe the pump–probe setup and the generation of the white-light probe. In Sec. III B, the methods of calibration and of determination of the angle of incidence and oxide layer parameters are presented.

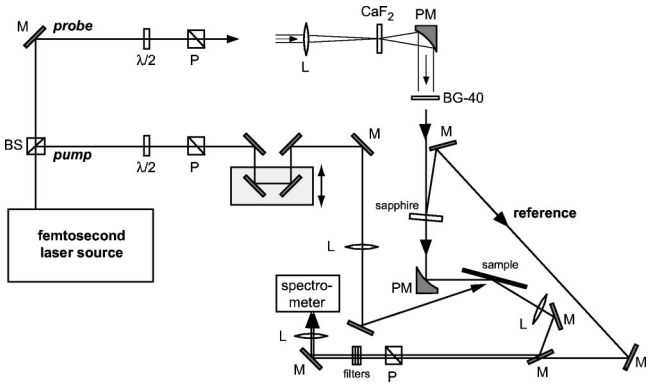

FIG. 5. Schematic representation of the white-light pump–probe setup. BS = polarizing beam splitter; M = flat mirror; PM = parabolic mirror; L = lens; P = polarizer; and λ/2 = half-wave plate.

A. White-light pump–probe setup

Figure 5 shows a schematic representation of the experimental setup. We use a commercially available Ti:sapphire oscillator to seed a home-built, 1 kHz repetition rate, Ti:sapphire multipass amplifier which produces 50 fs, 0.5 mJ pulses at 800 nm. The design of the amplifier follows that of Backus *et al.*[18]

As Fig. 5 shows, a femtosecond pulse is split into a pump and a probe pulse at the beamsplitter (BS). The pump pulse is directed to the sample via a variable delay stage, allowing for adjustable time delays between the pump and the probe pulse. The pump pulse is focused onto the sample using a slowly focusing lens (0.20 m focal length). The pump spot size can be adjusted according to specific experimental requirements by varying the distance from the lens to the sample, but remains at least four times larger than the probe spot to ensure probing of a homogeneously excited region. After the beamsplitter, the probe pulse passes through a waveplate–polarizer combination. The polarizer in the probe line is crossed to that of the pump line, and the waveplate-polarizer combination in each arm allows for adjustment of the probe- and pump-pulse energies.

A white-light probe pulse is generated by focusing the 800 nm pulse into CaF_2. A number of nonlinear optical processes, including self-focusing and self-phase modulation, contribute to the generation of this white-light continuum.[19] Due to the 10.2 eV band gap of CaF_2, the broadband continuum extends from the near infrared to the near ultraviolet.[20] As shown in Fig. 6, the majority of the probe pulse energy remains at the seed wavelength of 800 nm. A 1.5 mm Schott BG-40 filter is used to flatten the spectrum, making it suitable for charge-coupled-device spectrometer detection and preventing damage of the sample.

The broadband pulse is split into a probe and a ''reference'' pulse with a 1-mm-thick piece of sapphire. The probe pulse is focused on the sample with a parabolic mirror and recollimated with an acromatic lens. Both the probe and reference pulses are directed into a 1-to-1 imaging spectrometer. A broadband polarizer is inserted between the sample

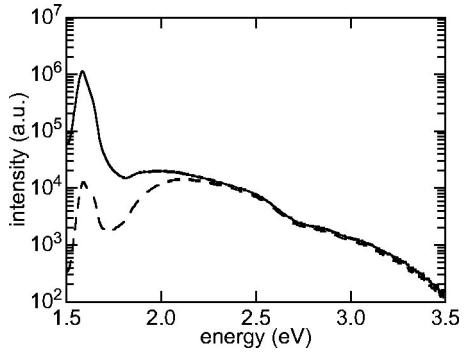

FIG. 6. Spectrum of the white-light generated in CaF_2. The solid and dashed curves show the spectrum of the white-light pulse before and after passing through the BG-40 filter, respectively.

and the spectrometer to prevent scattered pump light from reaching the detector and to ensure that only *p*-polarized light is measured. We monitor the reference pulse spectrum to correct for shot-to-shot probe fluctuations.

Maintaining femtosecond time resolution with the large bandwidth of the white-light probe pulses requires specific attention. While reflective optics are used to deliver the white-light pulse from the CaF_2 to the sample, the BG-40 filter and the CaF_2 itself contribute to dispersive stretching (chirp) of the probe. In order to regain the original time resolution, the measured reflectivities at each wavelength are time shifted to correct for this chirp. The chirp of our white-light probe pulse, measured using two-photon absorption,[21] is shown in Fig. 7. Pump–probe cross correlations using two-photon absorption indicate that the time resolution of the apparatus is no greater than 50 fs for all wavelengths of the probe.

B. Measuring absolute reflectivities

The constitutive relations in Sec. II relate the dielectric function to absolute reflectivity. This poses the experimental challenge of measuring the absolute reflectivity of a sample when reflective and transmissive optical elements modify the spectrum of the probe pulse before it reaches the detector. The calibration of the detection system must account for these absorptive losses. Since the probe and reference beams are split from the same pulse, the detected spectra $[S_{\mathrm{probe}}(\omega)$ and $S_{\mathrm{ref}}(\omega)]$ can be used to calibrate our system. For a particular sample, the ratio of the detected spectra is

$$\frac{S_{\mathrm{probe}}(\omega)}{S_{\mathrm{ref}}(\omega)} = \frac{g(\omega)}{h(\omega)} R(\omega), \tag{13}$$

where $h(\omega)$ accounts for the absorptive losses in the reference beamline and $g(\omega)$ accounts for the losses in the probe beamline, separate from the sample reflectivity $R(\omega)$. In order to calibrate the system we must measure $g(\omega)/h(\omega)$, which is independent of the sample under investigation. From the above equation,

$$\frac{g(\omega)}{h(\omega)} = \frac{S_{\mathrm{probe}}(\omega)}{S_{\mathrm{ref}}(\omega)} \frac{1}{R(\omega)}. \tag{14}$$

For a sample of known optical properties, we can calibrate the apparatus by measuring $S_{\mathrm{probe}}(\omega)$ and $S_{\mathrm{ref}}(\omega)$ and taking $R(\omega)$ to be the calculated reflectivity of the sample for a given angle of incidence. When multiple reference samples are used, the quality of the sample of interest can be verified and the confidence in the calibration can be improved.

The above-described method of calibration can also be used to measure the angle of incidence of the white-light probe and the thickness and dielectric constant of any oxide layers. To perform such a measurement, more reference samples are used than there are unknowns. All reference samples are aligned to the same (possibly unknown) angle of incidence using a HeNe laser. The values of $S_{\mathrm{probe}}/S_{\mathrm{ref}} \times 1/R(\omega)$ for different samples only agree when the reflectivity is calculated at the correct angle of incidence and with the correct oxide layer thicknesses and dielectric constant values. Using as many reference materials as unknowns ensures that all curves agree for only the correct values of the unknowns. Figure 8(a) is a plot of the uncertainty in the

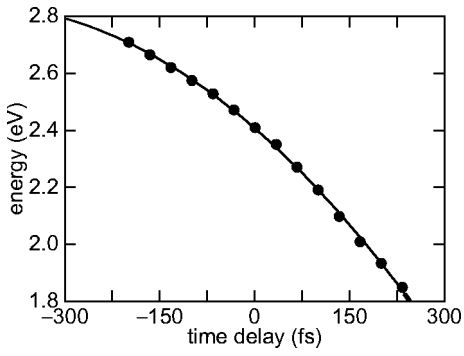

FIG. 7. Temporal chirp of the white-light pulse. The full circles indicate data points measured using two-photon absorption. The solid curve shows a second order polynomial fit through the data.

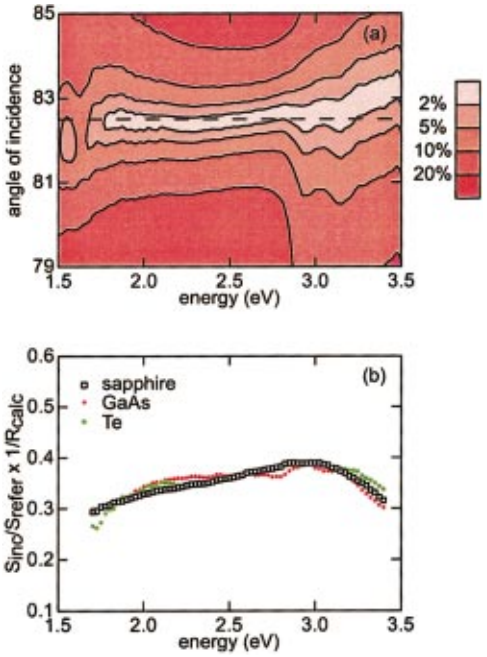

FIG. 8. (Color) (a) Contour plot of the uncertainty in the calibration as a function of photon energy for a range of possible angles of incidence. The best agreement occurs at 82.5° (dotted line), and the calibration is shown in (b).

calibration among three reference samples (standard deviation divided by mean) at each photon energy in the probe for a range of possible incident angles. The reference samples are sapphire, GaAs with an oxide layer of known thickness, and Te in the geometry of Fig. 4(a). The mean uncertainty is lowest for the angle indicated by the dotted line in Fig. 8(a), marking the actual angle of incidence of the probe (82.5°) for the case presented here. Figure 8(b) shows the agreement between the three samples for this angle of incidence. The calibration is taken to be the average of the three curves in Fig. 8(b). Using this method of analysis, the angle of incidence and oxide layer thicknesses can be determined to an accuracy of 0.1° and 0.5 nm, respectively. These uncertainties do not significantly affect the final assigned uncertainty in $\epsilon(\omega)$. They can be folded into the analysis of Sec. II to minimize their effects. Whenever possible, oxide layers are determined in a separate measurement to avoid the effects of parameter correlation.[7,22]

The uncertainty in measurements of the absolute reflectivity depend on both the accuracy of the calibration and shot-to-shot fluctuations of the probe. If the experiment is carried out at pump fluences below the threshold for permanent damage, multiple shots can be averaged at the repetition rate of the laser source. The resolution of our setup in this multiple-shot mode is better than $\Delta R/R = 10^{-3}$. However, this is not the accuracy in measuring the absolute reflectivity due to the approximate 1% uncertainty in the calibration. For experiments at pump fluences near or above the damage threshold, the sample must be translated between shots so that each pulse strikes a new spot on the sample. The single-shot operation mode carries larger uncertainties ($\Delta R/R \approx 5\%$) than that of the calibration because sample area limits the number of spectra that can be accumulated at each time delay and pump fluence. On the other hand, the dynamics of highly excited materials (e.g., the semiconductor-to-metal transitions in GaAs) are accompanied by signal variations of $\Delta R/R \approx 200\%$, so the signal-to-noise ratio is still high.

To calculate the uncertainty in $\epsilon(\omega)$, dielectric constant values for the four pairs of reflectivities $[R(\theta_1) \pm \Delta R(\theta_1), R(\theta_2) \pm \Delta R(\theta_2)]$ are extracted from the numerical inversion algorithm. Error bars are taken from the two values maximally displaced from the dielectric constant value associated with $[R(\theta_1), R(\theta_2)]$.

IV. TIME-RESOLVED DIELECTRIC FUNCTION MEASUREMENTS

As an illustration of our technique, we present measurements of the femtosecond time-resolved dielectric function for three representative materials: an isotropic material (GaAs), a thin film (a-GeSb), and an uniaxial material (Te). We briefly discuss the importance of these results and compare them to other measurements of the material dynamics.

A. Ultrafast carrier and lattice dynamics in GaAs

Shortly after the introduction of femtosecond laser sources, numerous experiments were conducted on semiconductors where a transition to a metallic state was observed upon laser irradiation. Experimental techniques included pump–probe reflectivity measurements,[23] both reflectivity and second harmonic measurements,[24–27] and pump–probe microscopy.[28,29] While a laser-induced phase transition was observed in each experiment with high precision, the nature of the resulting phase and the changes in the band structure were difficult to determine. This difficulty is due to the fact that many different values of $\epsilon(\omega)$, and hence many different band structures and material phases, can yield the same reflectivity at a particular angle of incidence.

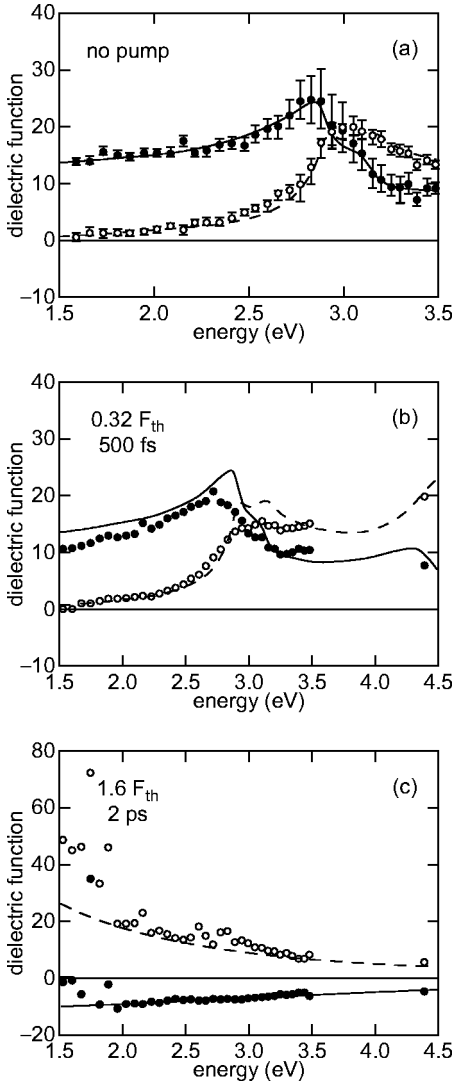

FIG. 9. Dielectric function data for GaAs — ●=Re[ϵ], ○=Im[ϵ]. (a) Under no excitation, $\epsilon(\omega)$ matches literature values of the dielectric function, represented by the solid and dashed curves (see Ref. 32). An example of changes in $\epsilon(\omega)$ due to the presence of excited carriers is shown in (b). (c) At sufficiently high pump fluences, a semiconductor-to-metal transition is observed, as evidenced by the fit to the Drude model ($\omega_p = 13.0$ eV and $\tau = 0.18$ fs).

We performed single-shot femtosecond time-resolved dielectric function measurements of GaAs to investigate carrier and lattice dynamics associated with its ultrafast semiconductor-to-metal transition under intense photoexcitation.[30,31] Figure 9 shows dielectric function measurements of GaAs. Without excitation of the sample, $\epsilon(\omega)$ matches literature values[32] of the dielectric function, confirming that our technique measures the dielectric function correctly. Figure 9(b) shows $\epsilon(\omega)$ 500 fs after excitation

below the threshold for permanent damage ($F_{th}=1.0$ kJ/m^2). Shortly after excitation, before the ions of the lattice can move, changes in $\epsilon(\omega)$ are due to the presence of excited carriers in the conduction band, which can be seen in the decrease of Im[$\epsilon(\omega)$] around the E_1 critical point. At higher excitation fluences, a transition to a metallic state is observed, an example of which is shown in Fig. 9(c). This data are well fit by the Drude model, which describes free-electron (metallic) behavior. The parameters of the fit (a plasma frequency of 13 eV and a relaxation time of 0.18 fs) reveal that virtually all of the valence electrons are free and that the band gap has completely collapsed. Theoretical calculations of the evolution of the dielectric function of GaAs after femtosecond-pulse excitation agree with our experimental results.[33–35]

B. Ultrafast phase changes in *a*-GeSb

The speed of ultrafast phase transitions and the large reflectivity variations associated with them make materials that display such transitions good candidates for optical switches and high speed optical data storage. Thin films of *a*-GeSb allow optically induced, optically reversible amorphous-to-crystalline transitions. In 1998, Sokolowski-Tinten and coworkers presented normal-incidence reflectivity measurements which suggested that femtosecond pulses above the threshold for permanent crystallization can induce an ultrafast *disorder-to-order* transition in amorphous $Ge_{0.06}Sb_{0.94}$ films within 200 fs.[36] The suggestion of a subpicosecond amorphous-to-crystalline phase transition raises an important question: how can lattice ordering occur in less time than it takes to establish thermal equilibrium between the laser-excited electrons and the lattice?

We performed single-shot dielectric function measurements of a 50 nm thin film of *a*-$Ge_{0.06}Sb_{0.94}$ to determine the nature of the phase during its ultrafast phase transition.[37] Figure 10(a) shows the agreement between $\epsilon(\omega)$ obtained at a time delay of -1 ps and literature values[32] of the dielectric function. As a reference, the dielectric function of the crystalline phase is also shown.[51] Because the film was optically thin and covered by a 1.25 nm SbO_2 oxide layer,[38] this sample is considered a four-medium system: air, oxide, *a*-GeSb thin film, and fused silica substrate.

Figure 10(b) shows the response of the dielectric function 200 fs after arrival of a pump pulse of fluence $F=320$ J/m^2, which is 60% above the threshold for permanent crystallization (F_{cr}). At this excitation fluence, the dielectric function remains unchanged from 200 fs to 475 ps. The same dielectric function is observed on subpicosecond time scales for all fluences above F_{cr}, indicating the existence of a nonthermal phase after femtosecond-pulse excitation. The existence of a new phase at ultrashort time delays for all fluences above F_{cr} was rightly identified by the authors of Ref. 36, however, the material is not crystalline, as evidenced by the discrepancy between the measured dielectric function and that of the crystalline phase [see Fig. 10(b)]. This discrepancy is brought out by Fig. 10(c), which shows the normal-incidence reflectivity as calculated from our time-resolved dielectric function measurements. Only at the 2.01 eV photon energy of the experiments in Ref. 38 does the reflectivity at 200 fs after excitation above F_{cr} match that of the crystalline phase. Furthermore, even at 2.01 eV, we find that for angles of incidence near or above the pseudo-Brewster, the reflectivity does not go to the crystalline level for pump fluences above F_{cr}. Our measurements thus show that broadband measurements of $\epsilon(\omega)$ enable one to distinguish phases that may appear the same based on reflectivity or transmission for a single photon energy at a single angle of incidence.

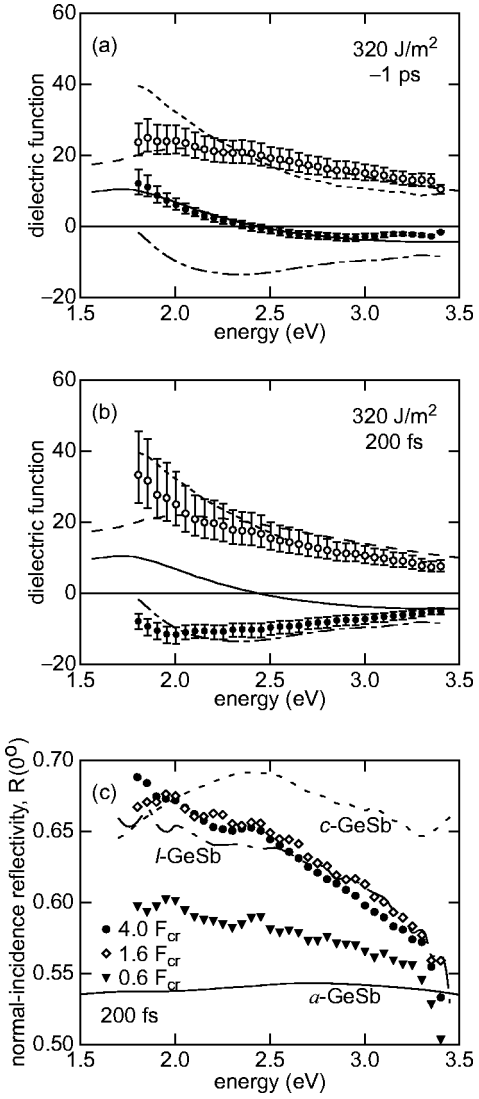

FIG. 10. (a),(b) Dielectric function data for *a*-GeSb thin films — ●=Re[$\epsilon(\omega)$], ○=Im[$\epsilon(\omega)$]: (a) $\epsilon(\omega)$ under no excitation (-1000 fs time delay), and (b) $\epsilon(\omega)$ 200 fs after excitation of 320 J/m^2. In both plots, the solid and dashed curves show the real and imaginary parts of $\epsilon(\omega)$ for the amorphous phase from previous measurements (see Ref. 50), and the dotted and dash-dotted curves show the real and imaginary parts of $\epsilon(\omega)$ of the crystalline phase. (c) Normal-incidence reflectivity calculated from the time-resolved $\epsilon(\omega)$ data.

C. Investigation of a displaced lattice: Coherent phonons in Te

Ultrashort-pulse excitation of Te instantaneously weakens lattice bonding, establishing new equilibrium lattice positions around which the lattice ions vibrate.[39–41] Because the phase of the generated lattice oscillations is the same in

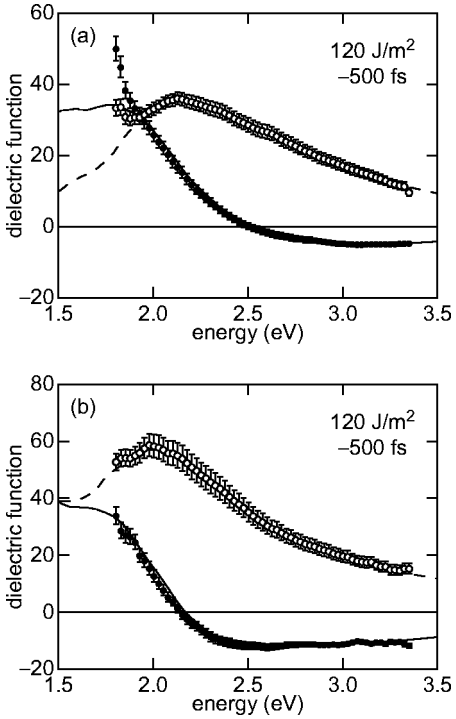

FIG. 11. Dielectric tensor data for Te — ● =Re[ϵ], ○=Im[ϵ]. At −500 fs time delay, both the (a) ordinary and (b) extraordinary dielectric function agree with literature values for the dielectric tensor, represented by the solid and dashed curves (see Ref. 32).

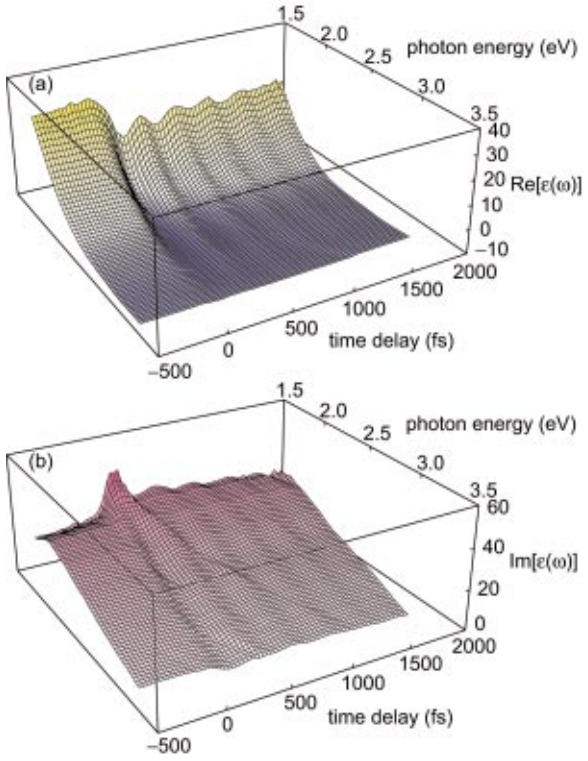

FIG. 12. (Color) Dynamics of the ordinary dielectric function of Te for excitation with a fluence of 120 J/m^2. Both (a) the real part and (b) the imaginary part show oscillatory behavior due the excitation of coherent phonons.

the entire pumped volume, probe pulses of shorter duration than the phonon period can be used to observe changes in the optical properties of Te (typically, $\Delta R/R \sim 10\%$) at different degrees of lattice distortion.[39,42] Experimental work by Bardeen[43] and others[44] found a pressure-induced semiconductor-to-metal transition in Te. These results coupled with investigations of coherent phonons in other materials[45] suggest that modification or even control of the phase (semiconducting versus semimetallic) of Te is possible at a rate equal to the phonon frequency ($\approx$3 THz) for pump fluences below the threshold for permanent damage. To investigate this possibility, we measured the response of Te with a multiple-shot acquisition system.[46]

Since Te is uniaxial, two independent elements of the dielectric tensor must be measured to fully characterize the ultrafast material response, as described in Sec. II B 2. Figure 11 shows the excellent agreement between measured and literature values[32] of both the ordinary and extraordinary dielectric functions. This agreement not only validates the technique for uniaxial materials, it also shows that no cumulative effects arise from operating in the multiple-shot mode where the sample is not translated between laser pulses. Because Te is a soft material, requiring a combined chemical and mechanical polishing process,[47] a small degree of surface roughness is unavoidable. To take this roughness into account, we assume a single layer between air and substrate, whose thickness varied depending on the sample quality of the probed region.[48] With a dielectric constant value of 5, the layer thickness varied from 5 to 10 nm among various data sets.

The dynamics of $\epsilon_{\mathrm{ord}}(\omega)$ are shown in Fig. 12. Within the error of the measurement, dielectric function values remain constant at all times before the pump arrives. After excitation, the oscillatory behavior of the optical properties indicate the presence of coherent phonons. A decaying offset from the initial values, separate from the oscillation, represents the relaxation of the equilibrium lattice spacing as electrons diffuse from the probed region. In contrast to reflectivity-only studies of coherent phonons in materials, the dielectric function data clearly indicate a shift of absorption resonances to lower photon energies. The broad resonance near 2 eV has moved to lower energies, as indicated by the shift in the peak of Im[$\epsilon_{\mathrm{ord}}(\omega)$] and the zero of Re[$\epsilon_{\mathrm{ord}}(\omega)$]. The magnitude and direction of the shift suggest that the lattice may be sufficiently displaced at the peak of the phonon oscillation to cross the conduction and valence bands, but that the short duration of the crossing could prohibit any metallic character from emerging.[46] In addition, we observe larger changes in $\epsilon_{\mathrm{ord}}(\omega)$ than in $\epsilon_{\mathrm{ext}}(\omega)$, which may be attributed to the fact that the motion of the coherent phonons is confined to the ab plane.

V. DISCUSSION

The time-resolved dielectric function measured with this reflectometry technique provides the most information of any linear optical probe, revealing changes in the lattice bonding, carrier distribution, and phase of a material. We avoid the necessity of assuming a particular model of the material dynamics as well as the potential pitfalls of other methods that measure changes in reflectivity at a single photon energy. While a representative set of sample types is presented, this

technique can be extended to any sample geometry, provided a constitutive relation between reflectivity and dielectric tensor exists.

An extension of this technique would be useful as a probe of the interaction between substrate and oxide layer. Under intense excitation, both above and below the threshold for permanent damage, the substrate can alter its lattice configuration or lose order completely. Yet, the dynamics of the oxide layer during the phase transition of the substrate are often ignored. Additional measurements at other angles of incidence could enable monitoring the substrate along with the thickness of the oxide layer and its optical properties. Given the accuracy of spectroscopic ellipsometry in measuring thin film characteristics, a pump-probe ellipsometer may be the ideal device for such an application because any change in oxide layer thickness, dielectric function, or in the oxide-substrate interface, is likely to be small on the picosecond time scale.

[1] I. S. Ruddock and D. J. Bradley, Appl. Phys. Lett. **29**, 296 (1976).
[2] T. Brabec and F. Krausz, Rev. Mod. Phys. **72**, 545 (2000).
[3] J. Shah, *Ultrafast Spectroscopy of Semiconductors and Semiconductor Nanostructures* (Springer, Berlin, 1996).
[4] A. H. Zewail, *Femtochemistry: Ultrafast Dynamics of the Chemical Bond* (World Scientific, Singapore, 1994).
[5] R. W. Collins, Rev. Sci. Instrum. **61**, 2029 (1990).
[6] S. N. Jasperson and S. E. Schnatterly, Rev. Sci. Instrum. **40**, 761 (1969).
[7] P. G. Snyder, M. C. Rost, G. H. Bu-Abbud, and J. A. Woollam, J. Appl. Phys. **60**, 3293 (1986).
[8] R. Greef, Rev. Sci. Instrum. **41**, 532 (1970).
[9] M. Born and E. Wolf, *Principles of Optics*, 6th ed. (Pergamon, Oxford, 1980).
[10] P. Y. Yu and M. Cardona, *Fundamentals of Semiconductors* (Springer, Berlin, 1996).
[11] D. Beaglehole, Proc. Phys. Soc. London **85**, 1007 (1965).
[12] H. Ehrenriech and H. R. Phillipp, Phys. Rev. **128**, 1622 (1962).
[13] R. F. Cohn, Appl. Opt. **29**, 304 (1990).
[14] W. H. Press, S. A. Teukolsky, W. T. Vetterling, and B. P. Flannery, *Numerical Recipes in C: The Art of Scientific Computing*, 2nd ed. (Cambridge University Press, New York, 1992).
[15] D. E. Aspnes, *Handbook of Optical Constants*, edited by E. D. Palik (Academic, New York, 1985).
[16] L. P. Mosteller, Jr. and F. Wooten, J. Opt. Soc. Am. **58**, 511 (1968).
[17] F. Wooten, Appl. Opt. **23**, 4226 (1984).
[18] S. Backus, J. Peatross, C. P. Huang, M. M. Murnane, and H. C. Kapteyn, Opt. Lett. **20**, 2000 (1995).
[19] G. Yang and Y. R. Shen, Opt. Lett. **9**, 510 (1984).
[20] A. Brodeur and S. L. Chin, J. Opt. Soc. Am. B **16**, 637 (1999).
[21] T. F. Albrecht, K. Seibert, and H. Kurz, Opt. Commun. **84**, 223 (1991).
[22] G. H. Bu-Abbud, N. M. Bashara, and J. A. Woollam, Thin Solid Films **138**, 27 (1986).
[23] C. V. Shank, R. Yen, and C. Hirlimann, Phys. Rev. Lett. **50**, 454 (1983).
[24] C. V. Shank, R. Yen, and C. Hirlimann, Phys. Rev. Lett. **51**, 900 (1983).
[25] P. Saeta, J.-K. Wang, Y. Siegal, N. Bloembergen, and E. Mazur, Phys. Rev. Lett. **67**, 1023 (1991).
[26] H. W. K. Tom, G. D. Aumiller, and C. H. Brito-Cruz, Phys. Rev. Lett. **60**, 1438 (1988).
[27] S. V. Govorkov, I. L. Shumay, W. Rudolph, and T. Schröder, Opt. Lett. **16**, 1013 (1991).
[28] M. C. Downer, R. L. Fork, and C. V. Shank, J. Opt. Soc. Am. B **2**, 595 (1985).
[29] K. Sokolowski-Tinten, J. Bialkowski, A. Cavalleri, D. von der Linde, A. Oparin, J. Meyer ter Vehn, and S. I. Anisimov, Phys. Rev. Lett. **81**, 224 (1998).
[30] J. P. Callan, A. M.-T. Kim, L. Huang, and E. Mazur, Chem. Phys. **251**, 167 (1998).
[31] L. Huang, J. P. Callan, E. N. Glezer, and E. Mazur, Phys. Rev. Lett. **80**, 185 (1998).
[32] E. D. Palik, *Handbook of Optical Constants of Solids* (Academic, New York, 1985).
[33] J. S. Graves and R. E. Allen, Phys. Rev. B **58**, 13627 (1998).
[34] R. E. Allen, T. Dumitrica, and B. Torralva, *Ultrafast Processes in Semiconductors*, edited by K.-T. Tsen (Academic, New York, 2000).
[35] L. X. Benedict, Phys. Rev. B **63**, 0752021 (2001).
[36] K. Sokolowski-Tinten, J. Solis, J. Bialkowski, J. Siegel, C. N. Afonso, and D. von der Linde, Phys. Rev. Lett. **81**, 3679 (1998).
[37] J. P. Callan, A. M.-T. Kim, C. A. D. Roeser, E. Mazur, J. Solis, J. Siegel, C. N. Afonso, and J. C. G. de Sande, Phys. Rev. Lett. **86**, 3650 (2001).
[38] J. C. G. de Sande, F. Vega, C. N. Afonso, C. Ortega, and J. Siejka, Thin Solid Films **249**, 195 (1994).
[39] T. K. Cheng, S. D. Brorson, A. S. Kazeroonian, J. S. Moodera, G. Dresselhaus, M. S. Dresselhaus, and E. P. Ippen, Appl. Phys. Lett. **57**, 1004 (1990).
[40] H. J. Zeiger, J. Vidal, T. K. Cheng, E. P. Ippen, G. Dresselhaus, and M. S. Dresselhaus, Phys. Rev. B **45**, 768 (1992).
[41] P. Tangney and S. Fahy, Phys. Rev. B **65**, 054302 (2002).
[42] S. Hunsche, K. Wienecke, T. Dekorsy, and H. Kurz, Phys. Rev. Lett. **75**, 1815 (1995).
[43] J. Bardeen, Phys. Rev. **75**, 1777 (1949).
[44] F. A. Blum and B. C. Deaton, Phys. Rev. **137**, 1410 (1965).
[45] T. K. Cheng, L. H. Acioli, J. Vidal, H. J. Zeiger, G. Dresselhaus, M. S. Dresselhaus, and E. P. Ippen, Appl. Phys. Lett. **62**, 1901 (1993).
[46] A. M.-T. Kim, C. A. D. Roeser, and E. Mazur, Phys. Rev. B (accepted).
[47] D. Fischer and P. Grosse, Z. Angew. Phys. **30**, 154 (1970).
[48] R. M. A. Azzam, and N. M. Bashara, *Ellipsometry and Polarized Light* (Elsevier North-Holland, New York, 1977).
[49] M. L. Cohen and J. Chelikowsky, *Electronic Structure and Optical Properties of Semiconductors*, 2nd ed. (Springer, Berlin, 1989).
[50] J. Solís, private communication (2001).
[51] Literature values of $\epsilon(\omega)$ for c-$Ge_{0.06}Sb_{0.94}$ are not available. The data presented are measurements taken in our apparatus of a region of the sample that was permanently crystallized by laser irradiation.